


## Clinching 1/2 scaling: Deciphering spreading data of droplet impact

Yufei Ma  and Haibo Huang <sup>\*</sup>

Department of Modern Mechanics, *University of Science and Technology of China*,  
Hefei, Anhui 230026, People's Republic of China

 (Received 8 May 2024; accepted 16 October 2024; published 8 November 2024)

In this study, we conduct numerical investigations into the impact of droplet collisions on solid surfaces, with a specific focus on the influence of wettability and initial diameter. Previous studies have proposed two distinct scaling laws, namely  $We^{1/2}$  and  $We^{1/4}$ , where  $We$  denotes the Weber number, to describe the maximum spreading diameter ratio in the capillary regime. Our energy analysis reveals that only the  $We^{1/2}$  scaling accurately characterizes the capillary regime. Additionally, we elucidate that the observed data slope of 1/4 arises from the  $We^{1/2}$  scaling while the initial diameter also plays a role within the low- $We$  range. To address this, we introduce a modified Weber number ( $We^*$ ), dependent on wettability, defined through energy conservation and accounting for the initial diameter *a priori*. Utilizing the  $We^*$ , we establish a generalized scaling for the maximum spreading diameter ratio, enabling the consolidation of numerical and experimental findings onto a single curve, regardless of wettability. Furthermore, this scaling demonstrates excellent agreement with numerical results for both low and relatively high- $We$  regimes but without splashing.

DOI: [10.1103/PhysRevFluids.9.113601](https://doi.org/10.1103/PhysRevFluids.9.113601)

### I. INTRODUCTION

The interaction between a liquid droplet and a solid surface is a phenomenon with widespread implications, manifesting in various natural processes and industrial applications. Examples include raindrop impact on soil [1], inkjet printing [2], self-cleaning surfaces [3], and bloodstain pattern analysis [4]. The droplet during impact can spread, rebound, or splash [5]. In the course of spreading, the droplet can attain its maximum spreading diameter  $D_{\max}$  (refer to Fig. 1). It is influenced by intrinsic droplet properties (viscosity  $\mu_H$ , surface tension  $\sigma$ , density  $\rho_H$ , and initial diameter  $D_0$ ), impact velocity  $U_0$ , and the surface wettability represented by the contact angle  $\theta$ . Consequently, the maximum spreading process is characterized by two crucial dimensionless parameters: the Weber number ( $We = \rho_H U_0^2 D_0 / \sigma$ ) and the Reynolds number ( $Re = \rho_H U_0 D_0 / \mu_H$ ). Additionally, the contact angle  $\theta$  plays a significant role in shaping the dynamics of this interaction.

Numerous theoretical models have emerged to predict the maximum spreading diameter ratio  $\beta_{\max} = D_{\max}/D_0$  of droplets impacting solid surfaces. These models, rooted in principles of energy or momentum conservation, meticulously balance the interplay among capillary, viscous, and inertial forces. Existing literature delineates two principal regimes: the viscous and capillary domains [6], where either capillary or viscous forces are deemed negligible for spreading. In the viscous regime,  $\beta_{\max}$  exhibits two scalings with  $Re^{1/4}$  [7] and  $Re^{1/5}$  [8] to balance viscous and inertial forces. Presently, the  $Re^{1/5}$  scaling in the viscous regime has undergone comprehensive theoretical and experimental validation [6,9,10]. In the capillary regime, Clanet *et al.* [6] proposed a scaling  $\beta_{\max} \propto We^{1/4}$  reconciling capillary and inertial forces through momentum conservation.

---

<sup>\*</sup>Contact author: [huanghb@ustc.edu.cn](mailto:huanghb@ustc.edu.cn)

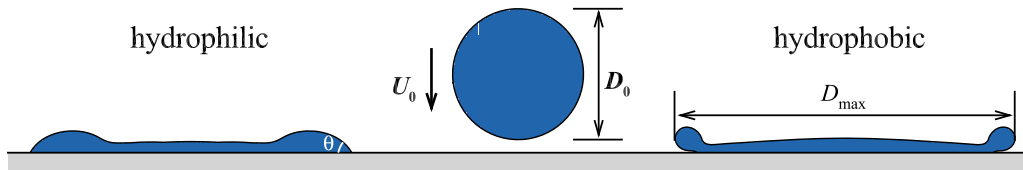


FIG. 1. A schematic diagram illustrating a droplet impacting a solid surface (middle) alongside snapshots depicting the maximum spreading of a hydrophilic droplet ( $\theta < 90^\circ$ ) on the left and a hydrophobic droplet ( $\theta > 90^\circ$ ) on the right. Here,  $\theta$  denotes the contact angle.

Alternatively, through energy conservation between surface- and kinetic energy, one can derive the scaling  $\beta_{\max} \propto We^{1/2}$  [9]. Laan *et al.* [4] contended that all three forces are significant when  $We$  and  $Re$  reach comparable values. They introduce a crossover scaling, uniting  $Re^{1/5}$  and  $We^{1/2}$ , in harmony with experimental data. Subsequently, Lee *et al.* [11] expanded upon this concept, incorporating considerations of surface wettability and roughness, thereby extending the applicability of the crossover scaling. Again, the effect of surface wettability was discussed in Ref. [12].

However, a persistent debate surrounds the two proposed scalings in the capillary regime. Initially introduced by Clanet *et al.* [6], the  $We^{1/4}$  scaling, derived from momentum or force balance, has been a subject of contention. For instance, there are concerns that the force balance may have been conducted in the non-Galilean reference frame of the drop [13,14]. Subsequently, a force balance for inertial impacts in a Galilean reference frame of the laboratory was performed by Villermaux *et al.* [13], yielding the  $We^{1/2}$  scaling. Then, Laan *et al.* [4] demonstrated that  $We^{1/4}$  performs effectively only for water drops, whereas  $We^{1/2}$  exhibits consistent behavior for drops of all liquids in their study. Consequently, they argued that  $We^{1/2}$  represents the correct scaling for the capillary regime, a standpoint validated by subsequent works such as Lee *et al.* [11] and a comprehensive review by Josserand *et al.* [5]. Despite this, the  $We^{1/4}$  scaling persists in the literature and finds agreement with results in studies [15–22]. It stimulates us to do this work and make some clarifications that in the capillary regime, the maximum spreading of drops is controlled by the balance between surface and kinetic energy, leading to the  $We^{1/2}$  scaling. As mentioned above, because both scalings show good agreement with experimental or numerical data, it is difficult to discriminate between them.

In this study, we tackle the aforementioned challenge by simulating droplet impacts on solid surfaces across a wide range of Weber numbers ( $We$ , 1–1000) and Reynolds numbers ( $Re$ , 10–10000), incorporating diverse wettabilities ( $\theta \sim 30^\circ$ – $150^\circ$ ). Our investigation rigorously assesses the validity of the  $We^{1/2}$  and  $We^{1/4}$  scalings within the capillary regime. Furthermore, we examine the influence of the initial diameter on these scaling models. Importantly, we also account for surface wettability, allowing us to establish a generalized scaling for  $\beta_{\max}$  under varying wettability conditions across both low and relatively high Weber numbers, building upon the findings of Laan *et al.* [4].

## II. METHODOLOGY AND VALIDATION

A schematic diagram illustrating a droplet's impact on a solid surface is presented in Fig. 1. The droplet, initially with a diameter  $D_0$ , descends with an initial impact velocity  $U_0$ . Surface wettability is characterized by the contact angle  $\theta$ . In our simulations, we employ the phase-field method [23,24] to model the two-phase fluid flow. The conservative phase-field equation, also known as the Allen-Cahn equation, is utilized for precise tracking of the fluid interface [14,25],

$$\frac{\partial \phi}{\partial t} + \nabla \cdot (\phi \mathbf{u}) = \nabla \cdot \left[ M(\nabla \phi - \frac{4}{\xi} \phi(1 - \phi) \hat{\mathbf{n}}) \right], \quad (1)$$

where  $\phi$  is the component variable ranging from 0 to 1, representing light (vapor) and heavy (liquid) fluids, respectively. The densities of these fluids are denoted as  $\rho_L$  and  $\rho_H$ .  $\mathbf{u}$  is the macroscopic

velocity vector,  $M$  is the mobility,  $\xi$  is the interface thickness, and  $\hat{\mathbf{n}}$  is the unit vector normal to the fluid interface, defined as  $\nabla\phi/|\nabla\phi|$  and pointing towards the liquid.

The isothermal, incompressible Navier-Stokes equations are used to simulate the flow,

$$\frac{\partial\rho}{\partial t} + \nabla \cdot (\rho\mathbf{u}) = 0, \quad (2)$$

$$\rho \left[ \frac{\partial\mathbf{u}}{\partial t} + \mathbf{u} \cdot \nabla(\mathbf{u}) \right] = -\nabla p + \nabla \cdot \{ \mu[\nabla\mathbf{u} + (\nabla\mathbf{u})^T] \} + \mathbf{f}_s, \quad (3)$$

where  $\rho$  is the local fluid density,  $\mu$  the dynamic viscosity,  $p$  the the macroscopic pressure, and  $\mathbf{f}_s$  the surface tension force, taking the form of  $\mathbf{f}_s = \mu_\phi \nabla\phi$  [23], where  $\mu_\phi$  is the chemical potential binary fluids.

In our simulations, the lattice Boltzmann method (LBM) [23,25] was adopted to solve the interface tracking Eq. (1):

$$h_\alpha(\mathbf{x} + \mathbf{e}_\alpha\delta t, t + \delta t) = h_\alpha(\mathbf{x}, t) - \frac{h_\alpha(\mathbf{x}, t) - h_\alpha^{\text{eq}}(\mathbf{x}, t)}{\tau_\phi + 1/2}, \quad (4)$$

where  $h_\alpha$  is the phase-field distribution function,  $\tau_\phi$  the phase-field relaxation time,  $\mathbf{e}_\alpha$  the discrete velocity, and  $h_\alpha^{\text{eq}}$  the equilibrium phase-field distribution function, which is defined as

$$h_\alpha^{\text{eq}} = \phi\Gamma_\alpha + w_\alpha \frac{M}{c_s^2} \left[ \frac{4}{W} \phi(1-\phi) \right] (\mathbf{e}_\alpha \cdot \hat{\mathbf{n}}), \quad (5)$$

where

$$\Gamma_\alpha = w_\alpha \left[ 1 + \frac{\mathbf{e}_\alpha \cdot \mathbf{u}}{c_s^2} + \frac{(\mathbf{e}_\alpha \cdot \mathbf{u})^2}{2c_s^4} - \frac{\mathbf{u} \cdot \mathbf{u}}{2c_s^2} \right], \quad (6)$$

and  $w_\alpha$  is the weight coefficient. The mobility  $M = \tau_\phi c_s^2 \delta t$ , and the speed of sound  $c_s = 1/\sqrt{3}$ . The component variable  $\phi$  is recovered by

$$\phi = \sum_\alpha h_\alpha, \quad (7)$$

and the density can be calculated by  $\rho = \rho_L + \phi(\rho_H - \rho_L)$ .

The Navier-Stokes equations (2) and (3) are solved by

$$\bar{g}_\alpha(\mathbf{x} + \mathbf{e}_\alpha\delta t, t + \delta t) = \bar{g}_\alpha(\mathbf{x}, t) + \Omega_\alpha(\mathbf{x}, t) + F_\alpha(\mathbf{x}, t), \quad (8)$$

where  $\bar{g}_\alpha$  is the hydrodynamic distribution function,  $\Omega_\alpha$  the multiple relaxation-time collision operator, taking the form of

$$\Omega_\alpha = -\Lambda_{\beta\alpha} (\bar{g}_\alpha - \bar{g}_\alpha^{\text{eq}}), \quad (9)$$

where  $\Lambda_{\beta\alpha}$  is the collision matrix, and

$$F_\alpha = \delta t [(\Gamma_\alpha - w_\alpha)(\rho_H - \rho_L)c_s^2 + \Gamma_\alpha \mu_\phi] (\mathbf{e}_\alpha - \mathbf{u}) \cdot \nabla\phi \quad (10)$$

is the forcing term. The modified equilibrium distribution function is defined by  $\bar{g}_\alpha^{\text{eq}} = g_\alpha^{\text{eq}} - F_\alpha/2$  and  $g_\alpha^{\text{eq}} = pw_\alpha + \rho c_s^2 (\Gamma_\alpha - w_\alpha)$ . The macrovariables are recovered through

$$\mathbf{u} = \frac{1}{\rho c_s^2} \sum_\alpha \bar{g}_\alpha \mathbf{e}_\alpha + \frac{\delta t}{2\rho} \mathbf{f}_s, \quad (11)$$

$$p = \sum_\alpha \bar{g}_\alpha + \frac{\delta t}{2} (\rho_H - \rho_L) c_s^2 \mathbf{u} \cdot \nabla\phi. \quad (12)$$

For more detailed information, please refer to Xiong *et al.* [25].

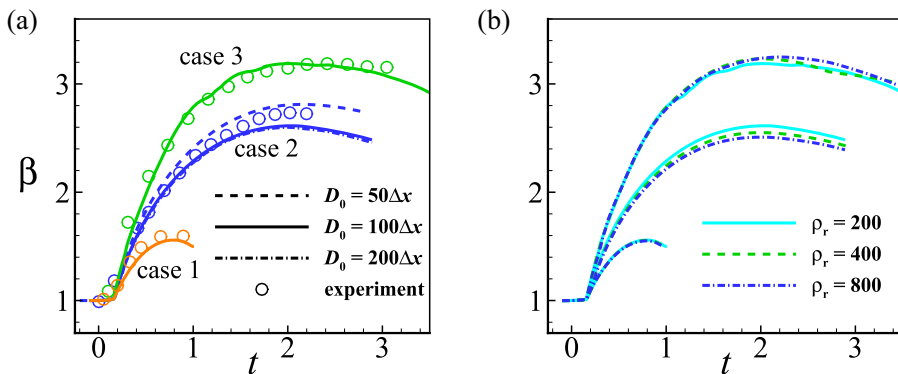


FIG. 2. (a) Evolution of the spreading ratio over time for three cases with a density ratio of  $\rho_r = 200$ :  $We = 6.8$ ,  $Re = 1000$ , and  $\theta = 116^\circ$  for case 1;  $We = 17.2$ ,  $Re = 658$ , and  $\theta = 54^\circ$  for case 2; and  $We = 120.7$ ,  $Re = 4200$ , and  $\theta = 121^\circ$  for case 3. Symbols represent experimental data from Lee *et al.* [29], while lines depict the corresponding numerical results. A grid-independence study is conducted for case 2. (b) Spreading ratio evolution over time for the same three cases, considering different  $\rho_r$  with  $D_0 = 100\Delta x$ . Notably,  $\rho_r = 800$  approximates the water and air scenario.

The present two-phase LBM shows nice numerical stability and accuracy to handle large-density contrast. However, these may depend on free numerical parameters such as the mobility  $M$  and interface thickness  $\xi$  [26]. It is generally more accurate to use smaller interfacial thickness but this may lead to numerical instabilities. A mobility that is too large can result in inaccurate results in turn. So, proper numerical parameters have to be determined in our simulation.

Concerning the substrate's wettability, the Neumann boundary condition [27] is utilized to enforce the contact angle. To enhance accuracy, we employ a weighted least-squares method [28]. Further details about the numerical method's implementation can be found in Xiong *et al.* [25]. Given the problem's symmetry, we apply symmetric boundary conditions, limiting our computational domain to a quarter of the physical problem's entirety. Apart from the specified boundaries, outflow boundary conditions are imposed on the remaining boundaries.

We aim to validate our numerical method initially. In all simulations, the computational domains are set at  $3D_0 \times 3D_0 \times 3D_0$  with a uniform Cartesian mesh. Figure 2(a) displays simulation results for three cases with different parameters from Lee *et al.* [29]. Through a grid-independence study using various resolutions ( $D_0 = 50\Delta x$ ,  $100\Delta x$ , and  $200\Delta x$ ), we determine that  $D_0 = 100\Delta x$  is sufficient for accurate results, as evidenced in case 2. This resolution is then adopted in subsequent simulations. Furthermore, our numerical results for the three cases exhibit excellent agreement with the experimental findings in Lee *et al.* [29], as illustrated in Fig. 2(a). Consequently, the numerical method employed to simulate droplet impact on solid surfaces is validated. It is noteworthy that in the above simulations, we choose a lower density ratio  $\rho_r = \rho_H/\rho_L = 200$  than that of water and air ( $\rho_r \approx 800$ ) to ensure computational stability. In fact, the impact of  $\rho_r$  on spreading is minimal, given that the vapor is too light to influence the liquid [30]. This is evident in Fig. 2(b), which illustrates that the discrepancies among the results for cases  $\rho_r = 200$ , 400, and 800 are very minor. Hence, the essential dynamics can be accurately captured with the present parameters.

### III. RESULTS AND DISCUSSION

The results depicting the maximum spreading diameter ratio,  $\beta_{\max}$ , as a function of  $Re$  with varying  $We$  and  $\theta$ , are presented in Fig. 3. In the viscous regime, characterized by high  $We$  where viscous forces dominate, the results at  $We = 1000$  consistently adhere to the  $\beta_{\max} \propto Re^{1/5}$  scaling across a wide range of  $Re$ . However, as  $We$  decreases, leading to an increased influence of capillary

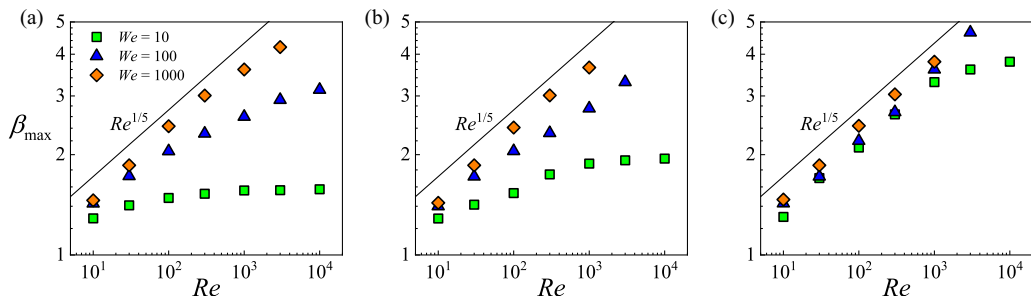


FIG. 3. The  $\beta_{\max}$  as a function of  $Re$  with different  $We$  and  $\theta$ : (a)  $\theta = 150^\circ$ , (b)  $\theta = 90^\circ$ , and (c)  $\theta = 30^\circ$ . The black lines represent the slope of  $Re^{1/5}$ .

forces at higher  $Re$  (possibly exceeding the viscous regime), the  $Re^{1/5}$  scaling holds mainly at low  $Re$  for cases with  $\theta = 150^\circ$  and  $90^\circ$  in Fig. 3. Notably, due to enhanced viscous effects on hydrophilic surfaces [21], Fig. 3(c) demonstrates that  $Re^{1/5}$  maintains effective scaling across a broad range of  $Re$  for  $\theta = 30^\circ$ , even at low  $We$ .

Hence, our numerical findings exhibit strong agreement with the  $Re^{1/5}$  scaling in the viscous regime under various wettability conditions. Nevertheless, our main emphasis lies in exploring the variations of  $\beta_{\max}$  with  $We$  in the capillary regime, and this will be discussed in the following.

### A. Capillary regime

In previous works, the capillary regime has been characterized differently based on the  $We^{1/2}$  and  $We^{1/4}$  scalings. Therefore, before studying the scaling within the capillary regime, it is crucial to determine the accurate description. To discern between the capillary and viscous regimes, an impact parameter  $P$  is first defined by Clanet *et al.* [6], based on  $We^{1/4}$  and  $Re^{1/5}$ . Then, the same approach is adopted by Laan *et al.* [4], which involves interpolating between  $Re^{1/5}$  and either  $We^{1/2}$  or  $We^{1/4}$  using  $\beta_{\max} Re^{-1/5} \propto f(P)$ . Here,  $P \in (0, \infty)$ , and  $f$  is a function of  $P$ . For the  $We^{1/2}$  or  $We^{1/4}$  scalings,  $P = WeRe^{-2/5}$  or  $WeRe^{-4/5}$ .

Figures 4(a), 4(b), and 4(c) show  $\beta_{\max} Re^{-1/5}$  as a function of different  $P$ . The data in Figs. 4(a) and 4(b) are obtained from our simulations with  $\theta = 150^\circ$ , while the data in Fig. 4(c) are from experimental results involving different liquids in Laan *et al.* [4]. According to  $We^{1/4}$  proposed by Clanet *et al.* [6], the transition between the two regimes is distinct and occurs around  $P = 1$  [see Fig. 4(a)] where  $P > 1$  denotes the viscous regime. In the viscous regime ( $P > 1$ ),  $\beta_{\max} Re^{-1/5}$  is almost constant, implying again that  $\beta_{\max} \propto Re^{1/5}$ . For  $P < 1$ ,  $\beta_{\max} Re^{-1/5}$  scales as  $P^{1/4}$  with  $P = WeRe^{-4/5}$ , leading to the recovery of  $\beta_{\max} \propto We^{1/4}$  in the capillary regime.

Contrastingly, Laan *et al.* [4] proposed a broad crossover regime between the two regimes based on the  $We^{1/2}$  scaling. The smooth crossover is modeled by a first-order Padé approximant,  $\beta_{\max} Re^{-1/5} = f_1(P) = P^{1/2}/(A + P^{1/2})$ , where  $P = WeRe^{-2/5}$  and  $A \sim O(1)$  is a fitting constant [Figs. 4(b) and 4(c)]. When  $P \gg A$ ,  $f_1$  scales as  $O(1)$  and  $\beta_{\max} \propto Re^{1/5}$  is recovered in the viscous regime. When  $P \ll A$ ,  $f_1$  scales as  $f_1(P) \propto P^{1/2}$  and the  $We^{1/2}$  scaling is recovered in the capillary regime [Fig. 4(b)].

In the following, we assess the two capillary regime descriptions using energy conversion distribution plots [10] at the maximum spreading [see Figs. 4(d) and 4(e)]. Due to energy conservation, initial energy (initial kinetic energy  $E_{k0}$  plus initial surface energy  $E_{s0}$ ) transforms into viscous dissipation  $E_d$ , surface energy  $E_s$ , and residual kinetic energy  $E_r$  at the maximum spreading. Here,  $E_d$ ,  $E_s$ , and  $E_r$  are obtained from our simulations. Generally, Fig. 4(d) shows that with increasing  $We$  or decreasing  $Re$ , and the viscous force becoming more significant,  $E_d$  increases while  $E_s$  decreases. Figure 4(e) shows that the distribution is also wettability dependent, which will be discussed in Sec. III C.

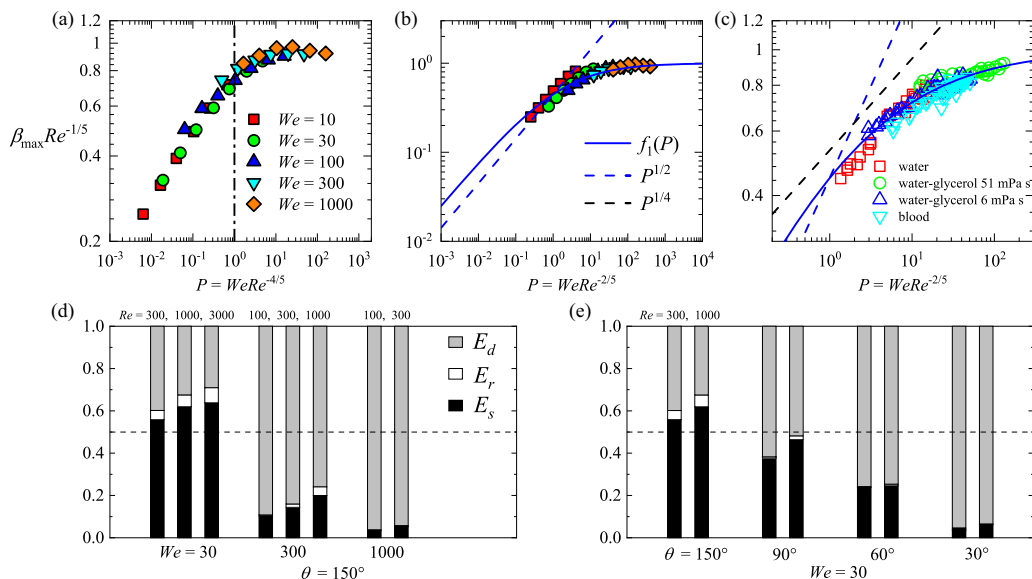


FIG. 4. The  $\beta_{\max} Re^{-1/5}$  as a function of the impact parameter  $P$  for our numerical results [ $P = WeRe^{-4/5}$  in (a) and  $P = WeRe^{-2/5}$  in (b)], alongside experimental results featuring different liquids from Laan *et al.* [4] (c), and the energy distribution at maximum spreading in our typical numerical results [(d), (e)]. In (a) and (b), all our numerical cases have  $\theta = 150^\circ$ . The blue solid lines represent the crossover scaling of  $f_1(P) = P^{1/2}/(A + P^{1/2})$  ( $A = 1.24$  is a fitting constant) from Ref. [4]. The blue and black dotted lines denote the  $1/2$  and  $1/4$  slopes, respectively. Each column in (d), (e) represents a case. The cases in (d) have  $\theta = 150^\circ$  but varying  $We, Re$ . The cases in (e) have  $We = 30$  with  $Re = 300$  or  $1000$  but varying wettability. Here,  $E_d$ ,  $E_s$ , and  $E_r$  represent viscous dissipation, surface energy, and residual kinetic energy at maximum spreading, respectively, all normalized by the sum of the initial kinetic energy and surface energy.

Now, let us focus on the descriptions of the viscous regime in Figs. 4(a) and 4(b), taking the cases of  $We = 1000$  with  $Re = 300$  and  $100$  as examples. In both cases,  $E_d$  dominates, while  $E_s$  is negligible [see Fig. 4(d)]. This aligns with the expected behavior in the viscous regime. In Figs. 4(a) and 4(b), the  $P$  values for the two cases are  $P = WeRe^{-4/5} \approx 10.4, 25.1$  and  $P = WeRe^{-2/5} \approx 102, 158$ , respectively. Clearly from the discussion above, both cases are in the viscous regime. Therefore, the energy conversion distribution plots confirm the viscous regimes described by both  $We^{1/2}$  and  $We^{1/4}$  models.

However, the descriptions of the capillary regime can significantly differ. For instance, for the two cases with  $Re = 3000$  and  $1000$  at  $We = 30$ , the  $We^{1/4}$  scaling suggests they are in the capillary regime [Fig. 4(a)], given  $P = WeRe^{-4/5} \approx 0.05, 0.12$ . On the other hand, Fig. 4(d) indicates that  $E_d$  is almost half of  $E_s$ , suggesting the viscous force is non-negligible, questioning their classification in the capillary regime. In contrast,  $We^{1/2}$  places these cases ( $P = WeRe^{-2/5} \approx 1.22, 1.89$ ) in the crossover regime, where both viscous and capillary forces are significant, aligning with the energy distribution plots. Thus, the definition of the capillary regime arising from  $We^{1/2}$  seems more reasonable, indicating that it is a better scaling law to balance capillary and inertial forces.

However, directly observing this scaling behavior in the data from previous literature proves challenging, considering the splashing with high impact velocity [5]. Conversely, the data slope of  $1/4$  is readily apparent [for instance, in the experimental data in Fig. 4(c)]. The reason may be that the extra viscous dissipation leads to a weaker dependence of the maximum spreading diameter on the impact velocity than would be expected from the  $We^{1/2}$  scaling. This dependence is, unfortunately, not very far from  $We^{1/4}$  for some liquids [see Fig. 4(c)]. In another way, we ascertain that the observed slope of  $1/4$  in Fig. 4(c) actually corresponds to the crossover regime rather than

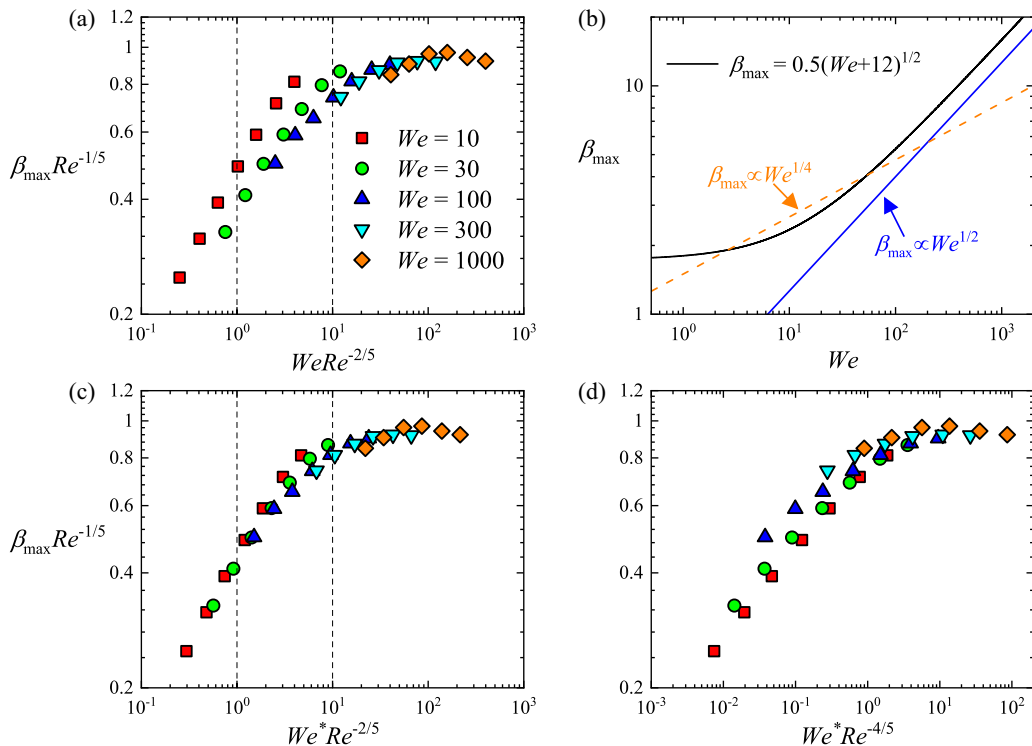


FIG. 5. The  $\beta_{\max} Re^{-1/5}$  as a function of  $WeRe^{-2/5}$  in (a),  $We^*Re^{-2/5}$  in (c), and  $We^*Re^{-4/5}$  in (d) for numerical results with various  $We$  and  $\theta = 150^\circ$ . (b) shows different Weber number trends of  $\beta_{\max}$ . The black line denotes the formula of  $\beta_{\max} \propto (We + 12)^{1/2}$ , specifically  $\beta_{\max} = 0.5(We + 12)^{1/2}$ , where the prefactor is arbitrary, and has little impact on the trend of this formula.

the capillary regime. Besides, another reason leading to the  $1/4$  slope is discussed in Sec. III B and may be attributed to the initial diameter. Moreover, it should be also noted that the observed  $We$  range is rather small, and the range of  $\beta_{\max}$  values is much too small to reliably fit the  $We^{1/4}$  scaling. Thus, we argue that these observations cannot be considered as evidence of the  $\beta_{\max} \propto We^{1/4}$  scaling in the capillary regime.

### B. Effect of initial diameter

By considering the energy balance of an impacting droplet in the capillary regime ignoring viscous dissipation, the  $We^{1/2}$  scaling can be established by comparing the initial energy  $E_{k0} + E_{s0} = (\pi/12)\rho_H U_0^2 D_0^3 + \pi\sigma D_0^2$  with surface energy  $E_s$  at the maximum spreading, where the droplet is approximately a pancake (see Fig. 1). Here,  $E_s$  at maximum spreading can be estimated as  $(\pi/4)\sigma D_{\max}^2 (1 - \cos\theta)$ , where the term  $(\cos\theta)$  accounts for the work done in expanding the wetted area [10,21]. For high  $We$ , the initial surface energy is negligible compared to the initial kinetic energy. Hence, we can equate  $E_{k0}$  with  $E_s$ . Consequently, for a fixed  $\theta$ , we obtain  $D_{\max} \propto D_0 \frac{\rho_H U_0^2 D_0}{\sigma} = D_0 We^{1/2}$ .

To validate  $We^{1/2}$ , Laan *et al.* [4] employed a method to assess whether the scaling could collapse the data points onto a single curve. To achieve this, we plotted the numerical results of  $\beta_{\max} Re^{-1/5}$  with a fixed  $\theta = 150^\circ$  against  $WeRe^{-2/5}$  (based on  $We^{1/2}$ ) in Fig. 5(a). Comparing this with the result in Fig. 4(a) (based on  $We^{1/4}$ ), the data in Fig. 5(a) collapse well for relatively high  $We$ , but fail to do so for low  $We$ , especially within the range between the two dashed lines. This discrepancy

may arise from the neglect of  $E_{s0}$ , which, as mentioned earlier, is non-negligible for low  $We$ . In other words, the initial diameter also plays a significant role in these cases. Consequently, considering the energy conversion  $E_{k0} + E_{s0} = E_s$ , leads to the equation

$$\beta_{\max} \propto \left( \frac{We + 12}{1 - \cos \theta} \right)^{1/2}. \quad (13)$$

The constant 12 is a consequence of  $E_{s0}$ , indicating the influence of the initial diameter. In the derivation, we have  $E_{k0} = E_{s0}$  when  $We = 12$ . Beyond this threshold,  $E_{k0}$  surpasses  $E_{s0}$ . Equation (13) indicates that at higher  $We$ ,  $\beta_{\max} \propto We^{1/2}$ . This assertion is corroborated by Fig. 5(b), where the solid black line [Eq. (13)] accurately depicts the trend of  $We^{1/2}$  for relatively higher  $We$ . It is important to note that (13) ignores viscous dissipation. If accounted for, the  $We^{1/2}$  trend would be observed at a much larger  $We$ . However, Josserand *et al.* [5] suggested that the available  $We$  range, where no splashing of drops occurs, does not permit observation of the  $We^{1/2}$  scaling. This explains the difficulty in directly observing this scaling behavior with data from droplets impacting no-slip substrates [see Fig. 4(c)]. However, Eq. (13) gradually deviates from  $\beta_{\max} \propto We^{1/2}$  as  $We$  decreases, as depicted in Fig. 5(b). It may be one of the reasons that  $We^{1/2}$  fails to collapse the data for low  $We$  [e.g.,  $We = 10$  in Fig. 5(a)].

From the analysis above, we understand that the inability to observe  $We^{1/2}$  stems from the impact of the initial diameter for low  $We$ , resulting in a data slope of  $1/4$  [Fig. 5(b)]. However, this cannot be regarded as evidence for  $\beta_{\max} \propto We^{1/4}$ . Additionally, it only holds within a very limited range of  $We$  as discussed in Sec. III A. Nonetheless, the scaling behavior in the capillary regime is fundamentally governed by  $We^{1/2}$ . Therefore, to account for the effect of the initial diameter, and similar to the way handling this in Pasandideh-Fard *et al.* [7], we define a modified Weber number  $We^*$  as.

$$We^* = \frac{We + 12}{1 - \cos \theta}, \quad (14)$$

which follows  $\beta_{\max} \propto (We^*)^{1/2}$  from (13) across the entire range of  $We$ . Subsequently,  $We^*$  (replacing  $We$ ) is utilized to collapse the same data from Fig. 5(a). The resulting collapse is depicted in Fig. 5(c), demonstrating a successful data collapse for both low and relatively high  $We$ . This indicates that the effect of the initial diameter is appropriately accounted for with such a modified Weber number. Furthermore, Fig. 5(d) illustrates that  $(We^*)^{1/4}$  results in a less satisfactory data collapse for low  $We$ . By comparing the results in Figs. 5(c) and 5(d), the  $We^{1/2}$  scaling is reconfirmed. Additionally, we conducted examinations for cases with different  $\theta$ , yielding consistent results. However, this aspect is not displayed here.

### C. Universal scaling

Based on Eq. (14), it is evident that  $We^*$  is contingent upon wettability. In this section, we try to utilize  $We^*$  to establish a generalized scaling law for  $\beta_{\max}$  concerning droplets impacting surfaces with diverse wettabilities, employing a methodology akin to that employed by Laan *et al.* [4]. From above analysis, in the capillary regime,  $\beta_{\max}$  scales with  $(We^*)^{1/2}$ . In the viscous regime, it adheres to  $Re^{1/5}$ . Thus, we express the interpolation between these two regimes as follows:

$$\beta_{\max} \propto Re^{1/5} f(P^*), \quad (15)$$

where  $P^* = We^* Re^{-2/5}$ . It is worth noting that as  $\theta$  decreases,  $P^*$  increases. And, a larger  $P^*$  means getting closer to the viscous regime. This finding aligns with the outcomes illustrated in Fig. 4(e), indicating a growing importance of viscous dissipation in energy distribution as  $\theta$  decreases. Hence,  $P^*$  effectively accounts for wettability. To seamlessly transition between these two regimes, we construct the function  $f$  using a first-order Padé approximant [4]:

$$\beta_{\max} Re^{-1/5} = (P^*)^{1/2} / (A + (P^*)^{1/2}), \quad (16)$$



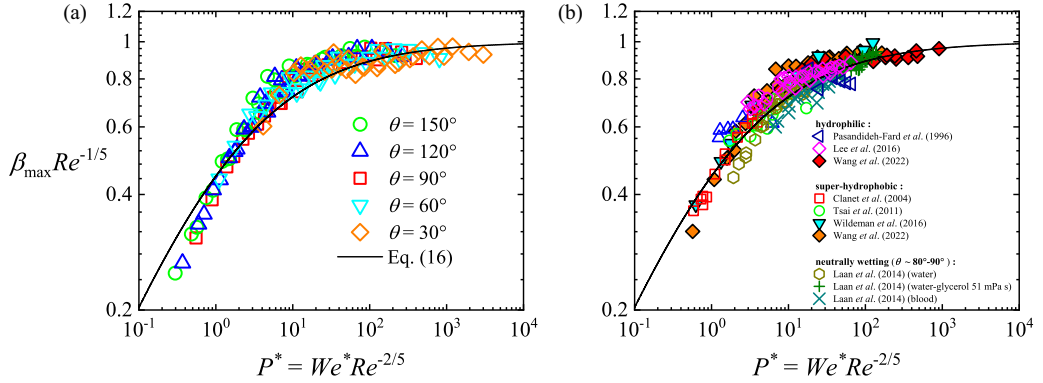


FIG. 6. The  $\beta_{\max} Re^{-1/5}$  as a function of  $We^* Re^{-2/5}$  with various wettabilities for numerical results (a) and results from previous works (b), where filled symbols are numerical data and others are experimental data. The black lines represent (16).

where  $A$  is a fitting constant. Figure 6(a) illustrates the numerical results of  $\beta_{\max} Re^{-1/5}$  versus  $P^*$  for various  $\theta$ , demonstrating a convergence of all data points onto a single curve. This curve closely aligns with Eq. (16), utilizing the same fitting constant as Laan *et al.* [4] ( $A = 1.24$ ). Furthermore, Fig. 6(b) presents results from various wettability conditions in previous studies, demonstrating consistent data collapse and alignment with the same curve. These support the notion that a generalized scaling of the maximum spreading for surfaces with different wettabilities can be achieved through (16).

As we know, the effects of initial diameter and wettability have been taken into account in Lee *et al.* [11]. However, our approach introduces a modified Weber number that incorporates the effects of initial diameter and wettability *a priori*, unlike the *a posteriori* determination of  $\beta_0$  in their work. This distinction is central to our contribution. Additionally, although Lee *et al.*'s scaling does not align with our data (as it assumes  $Re^{1/5}$  holds at any fixed  $We$ ), our proposed scaling is consistent with theirs, providing further validation for the  $We^{1/2}$  scaling.

In the following, we underscore the modification of the scaling model for predicting  $\beta_{\max}$ . Figure 7 presents a comparison between numerical results obtained with typical  $\theta$  values and different prediction models. While the present model (16) and Wang's model incorporate surface wettability, Lee's model does not. Consequently, as depicted in Fig. 7, Lee's model may not provide accurate predictions for cases with different  $\theta$ . Furthermore, unlike the present model, the other two models do not account for the initial-diameter effect. Consequently, they may fail to predict  $\beta_{\max}$  accurately at low  $We$ , potentially resulting in unphysical values of  $\beta_{\max} < 1$  as  $We$  decreases. The present model, however, exhibits good agreement with numerical results across a range of  $\theta$  values and  $We$ , representing a significant improvement over existing scaling models.

Apart from the modification of the scaling model, another contribution from this work emerges. We find the initial diameter plays an important role in judging the validation between  $We^{1/2}$  and  $We^{1/4}$  [see Figs. 5(a) and 5(c)], based on the method of Laan *et al.* [4]. Thus, we argue that a prediction model for the  $\beta_{\max}$  should always take the initial diameter into account, no matter whether with a low or high Weber number.

#### IV. CONCLUSIONS

The investigation explores the maximum spreading dynamics of droplets impacting solid surfaces across a spectrum of wettabilities, employing numerical simulations and literature data. A key focus lies in validating scaling laws within the capillary regime, revealing that only  $We^{1/2}$  accurately characterizes this domain. However, the initial-diameter effect hinders direct observation of this

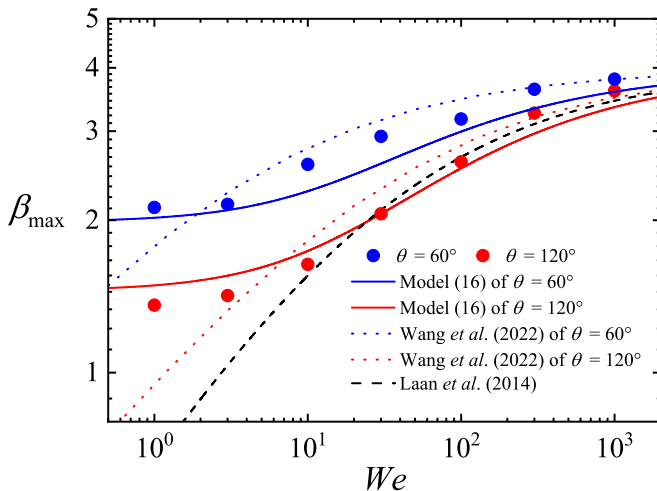


FIG. 7. Comparison of  $\beta_{\max}$  prediction models. Blue and red disks indicate  $\theta = 60^\circ$  and  $120^\circ$  cases, respectively. Solid lines depict the present model (16), while dotted lines represent the model of Wang *et al.* [21]. The black dashed line represents the model of Laan *et al.* [4], which disregards surface wettability.

scaling within the available  $We$  range. To address this, we introduce a modified Weber number  $We^*$ , facilitating  $\beta_{\max} \propto (We^*)^{1/2}$  across the entire capillary regime. Furthermore, utilizing  $We^*$ , we develop a generalized scaling model for  $\beta_{\max}$  accommodating diverse wettability conditions, demonstrating strong predictive capability across varying  $We$ . Last, we emphasize the necessity of considering the initial diameter in predictive models for maximum spreading diameter.

#### ACKNOWLEDGMENTS

This work was supported by the Natural Science Foundation of China (NSFC) Grant No. 12372253.

- 
- [1] Y. S. Joung and C. R. Buie, Aerosol generation by raindrop impact on soil, *Nat. Commun.* **6**, 6083 (2015).
  - [2] B. Derby, Inkjet printing of functional and structural materials: Fluid property requirements, feature stability, and resolution, *Annu. Rev. Mater. Res.* **40**, 395 (2010).
  - [3] R. Blossey, Self-cleaning surfaces—virtual realities, *Nat. Mater.* **2**, 301 (2003).
  - [4] N. Laan, K. G. de Bruin, D. Bartolo, C. Josserand, and D. Bonn, Maximum diameter of impacting liquid droplets, *Phys. Rev. Appl.* **2**, 044018 (2014).
  - [5] C. Josserand and S. T. Thoroddsen, Drop impact on a solid surface, *Annu. Rev. Fluid Mech.* **48**, 365 (2016).
  - [6] C. Clanet, C. Béguin, D. Richard, and D. Quéré, Maximal deformation of an impacting drop, *J. Fluid Mech.* **517**, 199 (2004).
  - [7] M. Pasandideh-Fard, Y. Qiao, S. Chandra, and J. Mostaghimi, Capillary effects during droplet impact on a solid surface, *Phys. Fluids* **8**, 650 (1996).
  - [8] I. V. Roisman, Inertia dominated drop collisions. II. An analytical solution of the Navier–Stokes equations for a spreading viscous film, *Phys. Fluids* **21**, 052104 (2009).
  - [9] J. Eggers, M. A. Fontelos, C. Josserand, and S. Zaleski, Drop dynamics after impact on a solid wall: Theory and simulations, *Phys. Fluids* **22**, 062101 (2010).

- [10] S. Wildeman, C. W. Visser, C. Sun, and D. Lohse, On the spreading of impacting drops, *J. Fluid Mech.* **805**, 636 (2016).
- [11] J. B. Lee, N. Laan, K. G. de Bruin, G. Skantzaris, N. Shahidzadeh, D. Derome, J. Carmeliet, and D. Bonn, Universal rescaling of drop impact on smooth and rough surfaces, *J. Fluid Mech.* **786**, R4 (2016).
- [12] T. C. de Goede, K. G. de Bruin, N. Shahidzadeh, and D. Bonn, Predicting the maximum spreading of a liquid drop impacting on a solid surface: Effect of surface tension and entrapped air layer, *Phys. Rev. Fluids* **4**, 053602 (2019).
- [13] E. Villermaux and B. Bossa, Drop fragmentation on impact, *J. Fluid Mech.* **668**, 412 (2011).
- [14] Y. Ma and H. Huang, Scaling maximum spreading of droplet impacting on flexible substrates, *J. Fluid Mech.* **958**, A35 (2023).
- [15] P. Tsai, M. H. Hendrix, R. R. Dijkstra, L. Shui, and D. Lohse, Microscopic structure influencing macroscopic splash at high Weber number, *Soft Matter* **7**, 11325 (2011).
- [16] H. R. Liu, C. Y. Zhang, P. Gao, X. Y. Lu, and H. Ding, On the maximal spreading of impacting compound drops, *J. Fluid Mech.* **854**, R6 (2018).
- [17] M. Damak and K. Varanasi, Expansion and retraction dynamics in drop-on-drop impacts on nonwetting surfaces, *Phys. Rev. Fluids* **3**, 093602 (2018).
- [18] W. Wang, C. Ji, F. Lin, J. Zou, and S. Dorbolo, Water drops bouncing off vertically vibrating textured surfaces, *J. Fluid Mech.* **876**, 1041 (2019).
- [19] P. García-Geijo, G. Riboux, and J. M. Gordillo, Inclined impact of drops, *J. Fluid Mech.* **897**, A12 (2020).
- [20] H. Zhan, C. Lu, C. Liu, Z. Wang, C. Lv, and Y. Liu, Horizontal motion of a superhydrophobic substrate affects the drop bouncing dynamics, *Phys. Rev. Lett.* **126**, 234503 (2021).
- [21] R. Wang, Y.-Z. Shi, C.-Y. Zhang, and H. Ding, On the maximal spreading of drops impacting onto a no-slip substrate, *Phys. Fluids* **34**, 052103 (2022).
- [22] Z. Zhang, C.-Y. Zhang, H.-R. Liu, and H. Ding, Impact dynamics of compound drops of fluids with density contrast, *J. Fluid Mech.* **964**, A34 (2023).
- [23] A. Fakhari and D. Bolster, Diffuse interface modeling of three-phase contact line dynamics on curved boundaries: A lattice Boltzmann model for large density and viscosity ratios, *J. Comput. Phys.* **334**, 620 (2017).
- [24] H. Liang, J. R. Xu, J. X. Chen, H. L. Wang, Z. H. Chai, and B. C. Shi, Phase-field-based lattice Boltzmann modeling of large-density-ratio two-phase flows, *Phys. Rev. E* **97**, 033309 (2018).
- [25] Y. F. Xiong, H. B. Huang, and X. Y. Lu, Numerical study of droplet impact on a flexible substrate, *Phys. Rev. E* **101**, 053107 (2020).
- [26] A. Fakhari, D. Bolster, and L.-S. Luo, A weighted multiple-relaxation-time lattice Boltzmann method for multiphase flows and its application to partial coalescence cascades, *J. Comput. Phys.* **341**, 22 (2017).
- [27] J. Shao, C. Shu, and Y.-T. Chew, Development of an immersed boundary-phase field-lattice Boltzmann method for Neumann boundary condition to study contact line dynamics, *J. Comput. Phys.* **234**, 8 (2013).
- [28] J.-H. Pan, M.-J. Ni, and N.-M. Zhang, A consistent and conservative immersed boundary method for MHD flows and moving boundary problems, *J. Comput. Phys.* **373**, 425 (2018).
- [29] J. B. Lee, D. Derome, R. Guyer, and J. Carmeliet, Modeling the maximum spreading of liquid droplets impacting wetting and nonwetting surfaces, *Langmuir* **32**, 1299 (2016).
- [30] A. Mazloomi Moqaddam, S. S. Chikatamarla, and I. V. Karlin, Drops bouncing off macro-textured superhydrophobic surfaces, *J. Fluid Mech.* **824**, 866 (2017).